Journal of Materials Chemistry C

PAPER

View Article Online
View Journal

Cite this: DOI: 10.1039/c8tc03303j

Effects of conjugated bridges on the photovoltaic properties of *ortho*-functionalized perylene diimides for non-fullerene polymer solar cells†

Jiazun Wu,‡[ab] Xiangchun Li,‡[c] Xiaodong Liu,*[ab] Shuanghong Wu,*[a] Wen-Yong Lai *[c] and Yonghao Zheng *[ab]

Received 5th July 2018,
Accepted 30th July 2018

DOI: 10.1039/c8tc03303j

rsc.li/materials-c

Perylene diimide (PDI) derivatives have great potential to replace the commonly used fullerene derivatives in bulk heterojunction (BHJ) polymer solar cells (PSCs). However, PDI-based molecules have a strong tendency to aggregate in thin films, which prevents the formation of appropriate phase separation. To alleviate this problem, much effort has been devoted to developing twisted PDI dimers with functional bridges at bay positions. Unfortunately, the bay-functionalized PDI dimers exhibit relatively low electron mobilities due to the excessive twist geometry. To solve this dilemma, an efficient method is to functionalize the PDI at less sterically-encumbered *ortho*-positions. In this article, we synthesized two novel *ortho*-functionalized PDI dimers, namely PDI-2Th-PDI and PDI-ThFTh-PDI, and investigated the influence of the conjugated bridge length on the physical and photovoltaic properties of PDIs. After introducing a fluorene bridge between the thiophene units, PDI-ThFTh-PDI with the extended conjugate length possessed a relatively low-crystalline nature and therefore exhibited one order of magnitude lower electron mobility compared to PDI-2Th-PDI. As a result, the power conversion efficiency (PCE) of solar cells fabricated with PDI-2Th-PDI as the electron acceptor and PTB7-Th as the electron donor is almost twice that of the solar cell with PDI-ThFTh-PDI as the acceptor. Our findings provide important guidelines for the design of more efficient *ortho*-functionalized PDI acceptors.

1. Introduction

Over the past few decades, bulk heterojunction (BHJ) polymer solar cells (PSCs) have attracted extensive interest owing to their distinguished advantages, such as low cost, light weight, solution processability and mechanical flexibility.[1–5] Fullerene derivatives, such as [6,6]-phenyl-C_{61}-butyric acid methyl ester ($PC_{61}BM$) and [6,6]-phenyl-C_{71}-butyric acid methyl ester ($PC_{71}BM$), are the most effective and widely used acceptor materials because of their strong electronegativity, high electron mobility and universal compatibility with multiple donor polymers.[1,6–10] To date, advances in efficient donor materials have led to a power conversion efficiency (PCE) of over 11% for single-junction polymer/fullerene-based PSCs.[11–13] Despite this remarkable success, further improvement was limited by the weak absorption at long wavelength, poor chemical and electronic tunability of fullerenes, and the metastable morphology in polymer:fullerene blends.[14–17] To resolve these drawbacks, a number of non-fullerene acceptors, including small molecules and polymers, have been explored to replace fullerene derivatives in BHJ PSCs.[11,18–36]

Among the various classes of non-fullerene acceptors, perylene diimides (PDIs) are one of the most promising alternatives due to their high electron mobility, strong absorption in the visible region, low synthesis cost and excellent stability.[19,33,37–46] Despite these favorable properties, PDI-based PSCs usually show low performance owing to the formation of large crystalline domains in the active layer, which is derived from the planar perylene core and their aggregation tendency.[37,39,47] To restrain the aggregation effects of PDIs, several approaches have been employed to reduce the strong π-stacking.[33,48] An effective method is the introduction of alkyl chains or aromatic groups at bay positions (1-, 6-, 7-, and 12-positions) or imide positions of the PDI molecules.[39,49–51] Another frequently used method is to develop twisted PDI dimers, in which two PDI units are linked at

[a] School of Optoelectronic Science and Engineering, University of Electronic Science and Technology of China (UESTC), Chengdu 610054, P. R. China. E-mail: xdliu@uestc.edu.cn, shwu@uestc.edu.cn, zhengyonghao@uestc.edu.cn
[b] Center for Applied Chemistry, University of Electronic Science and Technology of China (UESTC), Chengdu, 611731, P. R. China
[c] Key Laboratory for Organic Electronics and Information Displays (KLOEID) & Institute of Advanced Materials (IAM), Jiangsu National Synergetic Innovation Center for Advanced Materials (SICAM), Nanjing University of Posts & Telecommunications, 9 Wenyuan Road, Nanjing 210023, P. R. China. E-mail: iamwylai@njupt.edu.cn

† Electronic supplementary information (ESI) available. See DOI: 10.1039/c8tc03303j

‡ These authors contributed equally to this work.

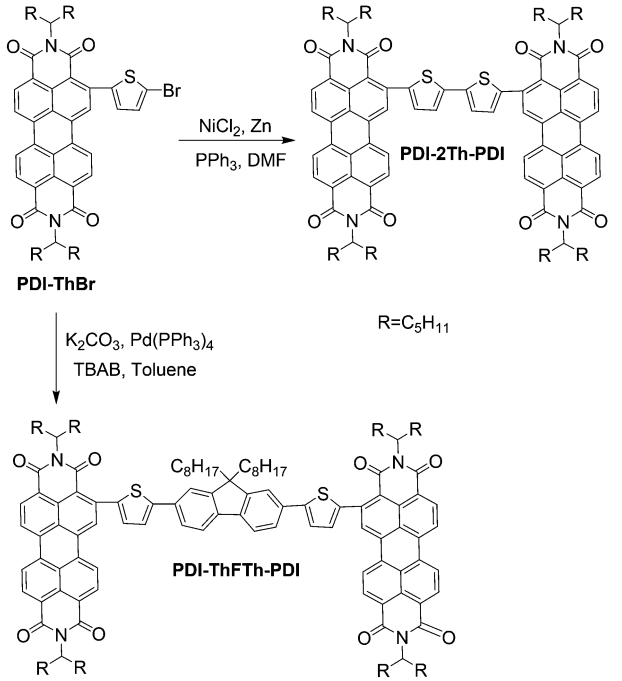

Scheme 1 Synthesis routes for the *ortho*-functionalized PDIs: PDI-2Th-PDI and PDI-ThFTh-PDI.

imide or bay positions either directly or through different linkage units.[51–54] Unfortunately, the bay-position functionalized PDI shows a lowered electron mobility due to its highly twisted molecular conformation.[38,48,55] Therefore, there is a trade-off between the suppression of molecular π–π stacking and the crystallinity of the blend layer.[56] To balance the trade-off, an attractive approach is to functionalize the less sterically encumbered *ortho*-positions (2-, 5-, 8-, and 11-positions). So far, only a few *ortho*-functionalized PDIs have been reported due to their complicated synthesis.[48,57] Recently, we reported a simple and low-cost method to synthesize desirable *ortho*-substituted PDIs, and we realized high-performance non-fullerene PSCs with a single PDI core as the acceptor.

In this work, we first investigated the effect of the conjugated bridge length on the physical and photovoltaic properties of *ortho*-functionalized PDIs. We designed two novel PDI dimers, PDI-2Th-PDI and PDI-ThFTh-PDI, with different bridge lengths (Scheme 1). Compared to PDI-ThFTh-PDI, PDI-2Th-PDI showed better crystallinity and thus higher electron mobility, which indicates that introducing a fluorene bridge between the thiophene units severely inhibited the crystallization of PDI molecules. When blending the PDI-2Th-PDI acceptor with a low-bandgap polymer donor PTB7-Th, the non-fullerene PSCs exhibited an impressive PCE of 4.00% without any solvent additives, which is significantly higher than that of the PSCs with PTB7-Th as the donor and PDI-ThFTh-PDI as the acceptor.

2. Experimental section

2.1. Fabrication of PSCs

OPV device fabrication. BHJ PSCs were fabricated with an inverted structure of ITO/ZnO/active layer/MoO_3/Ag. ITO-coated glass substrates (CSG Holding Co., Ltd, 10 ohm sq^{-1}) were cleaned stepwise with detergent, deionized water, acetone, and ethanol under sonication for 15 min each. The substrates were dried in a nitrogen stream and subjected to ultraviolet-ozone (UVO) treatment for 30 min to generate the hydrophilic surface. A sol–gel-derived ZnO electron transport layer was prepared according to literature procedures.[58,59] In brief, the ZnO precursor was prepared by dissolving zinc acetate dihydrate ($Zn(CH_3COO)_2{\cdot}2H_2O$, Sigma-Aldrich, >99.0%, 0.109 g) and ethanolamine ($NH_2CH_2CH_2OH$, Sigma-Aldrich, >99.5%, 32 μL) in 2-methoxyethanol ($CH_3OCH_2CH_2OH$, Sigma-Aldrich, 99.8%, anhydrous, 1 mL) under vigorous stirring for at least 12 h for the hydrolysis reaction in air. The ZnO precursor solution was filtered through a 0.45 μm nylon syringe filter and spin-cast onto the cleaned ITO substrate at 4000 rpm for 60 s. After being baked on a hot plate at 200 °C for 1 h in air, the samples were transferred into a nitrogen-filled glove box (<0.1 ppm O_2 and H_2O) for the rest of the device fabrication.

The active layer was spin-coated on the ZnO surface at different spin rates; PTB7-Th : PDI-2Th-PDI (1 : 2 w/w) and PTB7-Th : PDI-ThFTh-PDI (1 : 2 w/w) were dissolved in chlorobenzene with a total concentration ranging from 30 to 45 mg mL^{-1} and kept under stirring for at least 12 h before spin-coating the active layer. After spin-coating, the blend film was annealed on a hot plate at 120 °C for 5 min. To complete the device fabrication, 10 nm MoO_3 and 100 nm Ag were sequentially deposited by thermal evaporation at a base pressure of 5.0×10^{-5} Pa. The deposition rate and film thickness were monitored using a quartz crystal sensor. A shadow mask was put on the sample to define an active area of 4 mm^2 before the metal deposition.

SCLC mobility measurements. Space charge-limited currents (SCLCs) were tested in hole-only devices with a structure of ITO/PEDOT:PSS/active layer/MoO_3/Ag and electron-only devices with a structure of ITO/ZnO/active layer/Ca/Al. The devices were prepared following the identical procedure as described above for OPV devices, except that PEDOT:PSS was spin-coated on the ITO substrate instead of ZnO for hole-only devices and Ca/Al was deposited on the active layer instead of MoO_3/Ag for electron-only devices. The mobilities were determined by fitting the dark current to the modified Mott–Gurney equation[60,61]

$$J = \frac{9}{8}\varepsilon_0\varepsilon_r\mu_0\frac{V_{\mathrm{eff}}^2}{L^3}\exp\left(0.89\beta\sqrt{\frac{V_{\mathrm{eff}}}{L}}\right)$$

where ε_0 is the vacuum permittivity, ε_r is the relative dielectric constant of the active layer, μ_0 is the zero-field mobility of the charge carriers, and V_{eff} is the effective applied voltage, which is equal to the applied voltage minus the built-in potential originating from the work function difference between the electrodes, L is the thickness of the active layer, and β is the field-activation factor.

2.2. Characterization

The current density–voltage (J–V) characteristics were measured using a Keithley 2400 Source Meter unit under simulated

Air Mass 1.5 Global (AM 1.5 G) solar illumination at an intensity of 100 mW cm^{-2}, which was calibrated by a reference silicon solar cell. The measurements were carried out with the PSCs inside the glove box (<0.1 ppm O_2 and H_2O). The external quantum efficiency (EQE) spectra were measured using a QTEST HIFINITY 5 (Crowntech Inc., USA) at room temperature in air. The light intensity was calibrated using a single-crystal Si photovoltaic cell as a standard. Atomic force microscopy (AFM) measurements were conducted on an Asylum MFP-3D-BIO system (Oxford instruments) operating in tapping mode. Absorption spectra were acquired using a Shimadzu UV-2600 UV-vis spectrophotometer. Steady-state photoluminescence (PL) spectra were recorded on a Hitachi F-4600 fluorescence spectrophotometer. Cyclic voltammetry (CV) was performed in an electrolyte solution of 0.1 M tetrabutylammonium hexafluorophosphate in dichloromethane (DCM) at a scanning rate of 50 mV s^{-1}. The counter electrode was a platinum wire and the working electrode was a glassy carbon electrode. A silver wire coated with 0.1 M silver nitrate ($Ag/AgNO_3$) was used as a reference electrode in combination with the ferrocene–ferrocenium (Fc/Fc^+) redox couple as an internal standard. The vacuum level of Fc/Fc^+ was assumed to be −4.80 eV.

3. Results and discussion

3.1. Molecular design and synthesis

The synthetic procedures of PDI-2Th-PDI and PDI-ThFTh-PDI are depicted in Scheme 1. The synthesis method of PDI-ThBr was modified from our previous work,[38] which afforded the key intermediate in 41% yield. PDI-2Th-PDI was synthesized by a simple self-coupling reaction.[62–64] Suzuki coupling of PDI-ThBr and 9,9-dioctylfluorene-2-bis(boronic acid pinacol ester) occurred smoothly to give PDI-ThFTh-PDI in reasonable yields. The structures of all the compounds were characterized by mass spectroscopy, ^1H and ^{13}C NMR spectroscopy, and elemental analysis (ESI†). Thermogravimetric analysis (TGA) demonstrated the good thermal stability of PDI-2Th-PDI and PDI-ThFTh-PDI with temperatures of 5% weight loss at 352 °C and 379 °C, respectively, as shown in Fig. S1 (ESI†).

3.2. Physical properties of PDI-2Th-PDI and PDI-ThFTh-PDI

Fig. 1a shows the normalized UV-vis absorption spectra of PDI-2Th-PDI and PDI-ThFTh-PDI in DCM solution. Both of the molecules show broad absorption bands in the wavelength range from 300 to 550 nm, with a complete spectral overlap in the range of 445–550 nm that is attributed to the PDI segment absorption.[10,65] In the range of 300–445 nm, PDI-ThFTh-PDI exhibits a stronger absorption than PDI-2Th-PDI due to the extended π-conjugation length as a result of the incorporation of the fluorene unit. Fig. 1b depicts the UV-vis spectra of the donor polymer PTB7-Th, two PDI acceptors and PTB7-Th/acceptor mixtures in the film state. The thin-film absorption spectra of the two PDI acceptors are broadened and red-shifted relative to their solution spectra, covering a broad absorption range from 300 to 650 nm. The absorption spectrum of the

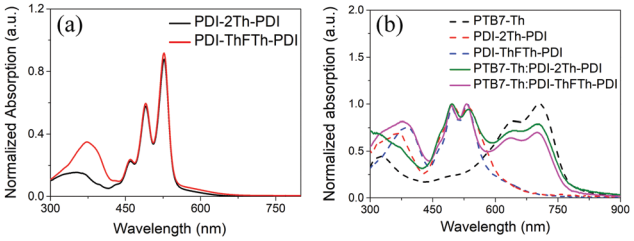

Fig. 1 UV-vis absorption spectra of PDI-2Th-PDI and PDI-ThFTh-PDI (a) in DCM and (b) in films cast without blending and with blended PTB7-Th.

PTB7-Th thin film exhibits a low-bandgap absorption in the region of 550–750 nm, which complements well with the absorption of our PDI electron acceptors.[66] The PTB7-Th:acceptor blend films show wide absorption bands spanning almost the whole visible spectrum, which probably results in high short-circuit current density (J_{sc}) values.

To study the exciton dissociation efficiency at the donor/acceptor hetero-interface, the PL spectra of the PTB7-Th:acceptor blend films were measured and compared with the neat PTB7-Th and two PDI acceptor films, as shown in Fig. S2 (ESI†). The PL of the PTB7-Th:acceptor blends is significantly quenched relative to the PL intensity of the pure PTB7-Th film when excited at 620 nm where only PTB7-Th is excited (Fig. S2a, ESI†), which indicates the efficient electron transfer process from PTB7-Th to the PDI acceptors. Upon excitation at 490 nm, where only the PDI acceptor is excited, the PTB7-Th:PDI-2Th-PDI blend film shows a higher PL quenching efficiency compared to the PTB7-Th:PDI-ThFTh-PDI blend film (Fig. S2b, ESI†), thus implying a more efficient hole transfer from PDI-2Th-PDI to PTB7-Th than that from PDI-ThFTh-PDI to PTB7-Th.[67]

3.3. Photovoltaic performance of PTB7-Th:PDI acceptor-based PSCs

To demonstrate the potential of the two PDI derivatives as electron acceptors, we fabricated BHJ PSCs in an inverted device architecture of ITO/ZnO/PTB7-Th:acceptor/MoO_3/Ag, where ZnO and MoO_3 were applied individually as the cathode and anode interlayers. Fig. 2a and b show the inverted device structure and the energy levels of the component materials, respectively. The highest occupied molecular orbital (HOMO) and lowest unoccupied molecular orbital (LUMO) energy levels of the two PDI acceptors were determined by CV, and the results are shown in Fig. S3 and Table S1 (ESI†). The HOMO/LUMO levels of PDI-2Th-PDI and PDI-ThFTh-PDI are almost the same, located at −5.73/−3.79 eV and −5.71/−3.81 eV, respectively, which indicates that introducing a fluorene unit does not affect the energy levels of our PDI system. Computational studies by density functional theory (DFT) were additionally performed. The dihedral angles between the two constituent PDI units were calculated to be 7° for PDI-2Th-PDI and 0° for PDI-ThFTh-PDI, which demonstrates that the structures of the two PDI molecules are almost planar (Fig. S4b, ESI†). As shown in Fig. S4c (ESI†), the HOMO/LUMO levels obtained from DFT calculations are in good agreement with the experimental results estimated from CV. As expected,

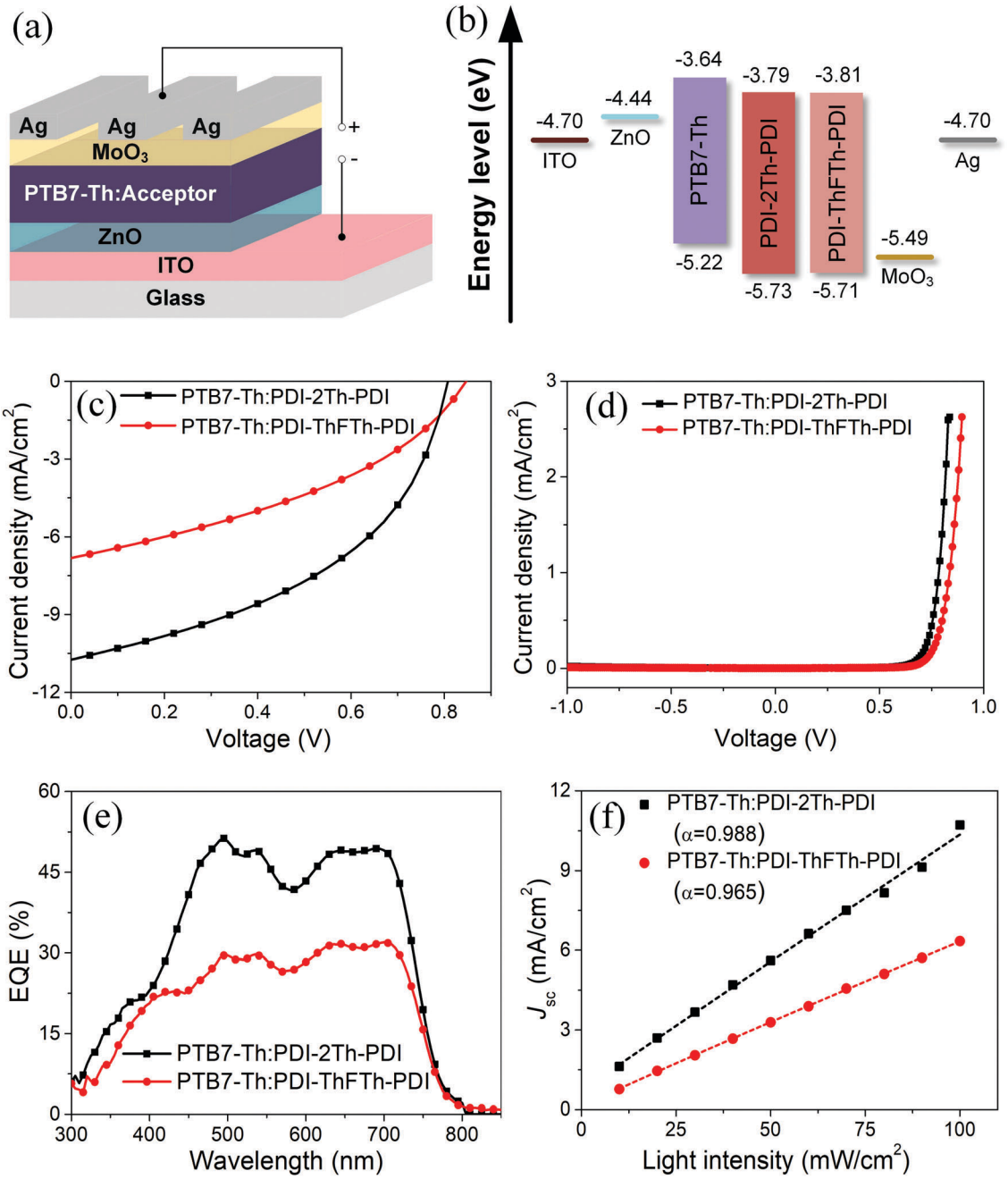

Fig. 2 (a) Schematic illustration of the PSCs studied in this work. (b) Energy-level diagram for each component of the devices. (c and d) *J*–*V* characteristics for PTB7-Th:PDI-2Th-PDI and PTB7-Th:PDI-ThFTh-PDI-based solar cells (c) under illumination of AM 1.5 G, 100 mW cm^{-2} and (d) in the dark. (e) EQE curves of the corresponding devices. (f) Light intensity dependence of the short-circuit current density of the devices.

the HOMO–LUMO map of both molecules suggests that the HOMO and LUMO orbitals locate at the conjugated bridge and the PDI cores, respectively. In addition, the bridge length of PDI-2Th-PDI is 9 Å, which is shorter than that (17 Å) of PDI-ThFTh-PDI.

Fig. 2c shows the *J*–*V* characteristics of the optimized devices based on two PDI acceptors (and PTB7-Th as the donor) under illumination of AM 1.5 G, 100 mW cm^{-2}, and Table 1 lists the photovoltaic parameters of the corresponding PSCs for a clear comparison. The details of the systematic device optimization, such as the donor/acceptor (D/A) blend ratio, photoactive layer thickness and thermal annealing temperature, are presented in Fig. S5–S7 and Tables S2–S4 (ESI†). The PSCs based on PTB7-Th:PDI-2Th-PDI achieved a high PCE of 4.00%, with a J_{sc} of 10.72 mA cm^{-2}, an open-circuit voltage (V_{oc}) of 0.81 V, and a fill factor (FF) of 46.0%. In contrast, the PSCs based on PTB7-Th:PDI-ThFTh-PDI possessed a relatively low PCE of 2.22%, with a J_{sc}, V_{oc} and FF of 6.81 mA cm^{-2}, 0.84 V and 39.0%, respectively. For both of these two PDI acceptors, the optimized D/A blend weight ratio is 1 : 2, and only a simple thermal

Table 1 Photovoltaic performance of the PSCs based on PTB7-Th:PDI-2Th-PDI and PTB7-Th:PDI-ThFTh-PDI under illumination of AM 1.5 G, 100 mW cm^{-2}

Active layer	V_{oc}[a] (V)	J_{sc}[a] (mA cm^{-2})	FF[a] (%)	PCE[a] (%)	J_{sc}[b] (mA cm^{-2})
PTB7-Th:PDI-2Th-PDI	0.81 (0.81 ± 0.01)	10.72 (10.08 ± 0.38)	46.0 (46.7 ± 0.6)	4.00 (3.82 ± 0.10)	10.50
PTB7-Th:PDI-ThFTh-PDI	0.84	6.81 (6.47 ± 0.24)	39.0 (39.3 ± 0.5)	2.22 (2.14 ± 0.06)	6.79

[a] The best values are given, followed by the averages and standard deviations in parentheses, calculated from at least eight devices. [b] J_{sc} calculated from the EQE spectrum.

annealing procedure is employed to optimize the active layer morphology, without using any additives. Fig. 2d presents the dark *J–V* characteristics of the optimized devices based on two PDI acceptors. The PTB7-Th:PDI-ThFTh-PDI device exhibits a higher turn-on voltage than that of the PTB7-Th:PDI-2Th-PDI device, indicating a larger built-in potential across the device, and thus a higher V_{oc} of the PTB7-Th:PDI-ThFTh-PDI PSC.

To confirm the accuracy of the photon *J–V* measurements of the devices, their corresponding EQE spectra are presented in Fig. 2e. An enhanced efficiency is observed throughout the full visible spectral range from 300 to 800 nm for the PTB7-Th:PDI-2Th-PDI device when compared to the PTB7-Th:PDI-ThFTh-PDI device, which is consistent with the variation trend of J_{sc} values obtained from the *J–V* characteristics. By integrating the product of the EQE data with the AM 1.5 G solar photon flux, the calculated J_{sc} values for the PTB7-Th:PDI-2Th-PDI and PTB7-Th:PDI-ThFTh-PDI devices are 10.50 and 6.79 mA cm^{-2}, respectively, which are very close to the measured values from the *J–V* curves shown in Table 1.

The dependence of *J–V* characteristics on light intensity (P_{light}) can give information on the recombination loss of devices.[52] In principle, J_{sc} has a power-law dependence on P_{light}, which can be expressed as $J_{sc} \propto (P_{light})^{\alpha}$, where the power-law component (α) should be unity when the bimolecular recombination in the device is negligible.[67,68] Fig. 2f illustrates J_{sc} as a function of P_{light} for the optimized devices based on two PDI acceptors. The extracted α values are 0.988 and 0.965 for the PTB7-Th:PDI-2Th-PDI and PTB7-Th:PDI-ThFTh-PDI devices, respectively. This result indicates that the bimolecular recombination was significantly suppressed in the PSCs with PDI-2Th-PDI as the acceptor.

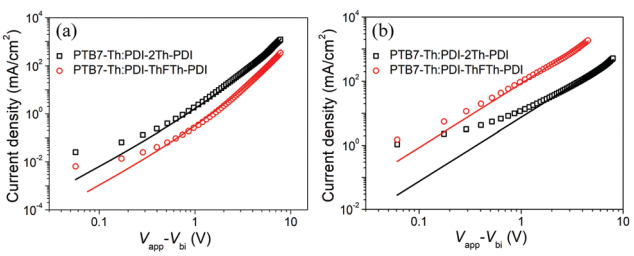

Fig. 3 *J–V* characteristics in the dark of (a) electron-only devices in the configuration of ITO/ZnO/active layer/Ca/Al and (b) hole-only devices in the configuration of ITO/PEDOT:PSS/active layer/MoO_3/Ag. The symbols represent experimental data, and the solid lines are the fit to the experimental data by the modified Mott–Gurney equation. The applied voltage is corrected for the built-in potential due to the work function difference of the two electrodes.

3.4. Charge transport properties of PTB7-Th:acceptor blend films

According to the above study, the much better performance of the PTB7-Th:PDI-2Th-PDI device, in comparison with the PTB7-Th:PDI-ThFTh-PDI device, can be attributed to the higher J_{sc} and FF originating from the reduced bimolecular recombination. To gain more insight into the remarkably high J_{sc} and FF of the PTB7-Th:PDI-2Th-PDI device, the charge transport properties of the optimized PTB7-Th:acceptor blend films were investigated using the SCLC method with the device structures of ITO/ZnO/active layer/Ca/Al for electron and ITO/PEDOT:PSS/active layer/MoO_3/Ag for hole transport measurements.[57,66] Fig. 3a and b, respectively, show the dark *J–V* curves, plotted on a log–log scale, of the electron-only and hole-only devices based on two PDI acceptors. The charge carrier mobilities of the blend films were extracted by fitting the *J–V* curves in the near quadratic region according to the modified Mott–Gurney equation.[60,61] Table 2 gives the estimated electron and hole mobilities. The electron mobility (μ_e) of the PTB7-Th:PDI-2Th-PDI blend film (1.10×10^{-4} cm^2 V^{-1} s^{-1}) is one order of magnitude higher than that of the PTB7-Th:PDI-ThFTh-PDI blend film (1.34×10^{-5} cm^2 V^{-1} s^{-1}), whereas the hole mobility (μ_h) of the PTB7-Th:PDI-2Th-PDI blend film (4.33×10^{-4} cm^2 V^{-1} s^{-1}) is almost one order of magnitude lower than that (3.40×10^{-3} cm^2 V^{-1} s^{-1}) of the PTB7-Th:PDI-ThFTh-PDI blend film. As a result, the PTB7-Th:PDI-2Th-PDI blend possessed a much more balanced μ_h/μ_e (3.9) compared to that (253.7) of the PTB7-Th:PDI-ThFTh-PDI blend, which can explain the reduced bimolecular recombination, and therefore the enhanced J_{sc} and FF of the PTB7-Th:PDI-2Th-PDI device.[69]

3.5. Morphological characterization of the active layers

The morphology of the active layer is an important factor in determining the charge separation and transport, and thus it affects the carrier mobilities in the blend films.[69,70] The ideal BHJ morphology contains a bi-continuous interpenetrating network of pure donor and acceptor domains that are smaller than the typical exciton diffusion length of less than 10 nm.[71,72] The surface morphology of our PTB7-Th:acceptor blend films was investigated by AFM imaging. The AFM height and phase images (2×2 μm^2) are shown in Fig. 4. The PTB7-Th:PDI-2Th-PDI blend film exhibits a network of fibrils with diameters of ~40 nm, which should favor a high exciton dissociation efficiency (Fig. 4c).[73] The fine surface morphology is consistent with the efficient PL quenching of the blend film. In contrast, a less defined phase separation was found for the PTB7-Th:PDI-ThFTh-PDI blend (Fig. 4d). The root-mean-square (RMS) for

Table 2 Calculated hole mobilities, electron mobilities, and hole-to-electron-mobility ratios for PTB7-Th:PDI-2Th-PDI and PTB7-Th:PDI-ThFTh-PDI-based devices. The thicknesses and root-mean-square (RMS) surface roughnesses of the two blend films are also listed

Active layer	Thickness (nm)	μ_h ($cm^2\ V^{-1}\ s^{-1}$)	μ_e ($cm^2\ V^{-1}\ s^{-1}$)	μ_h/μ_e	RMS (nm)
PTB7-Th:PDI-2Th-PDI	120	4.33×10^{-4}	1.10×10^{-4}	3.9	0.95
PTB7-Th:PDI-ThFTh-PDI	106	3.40×10^{-3}	1.34×10^{-5}	253.7	1.37

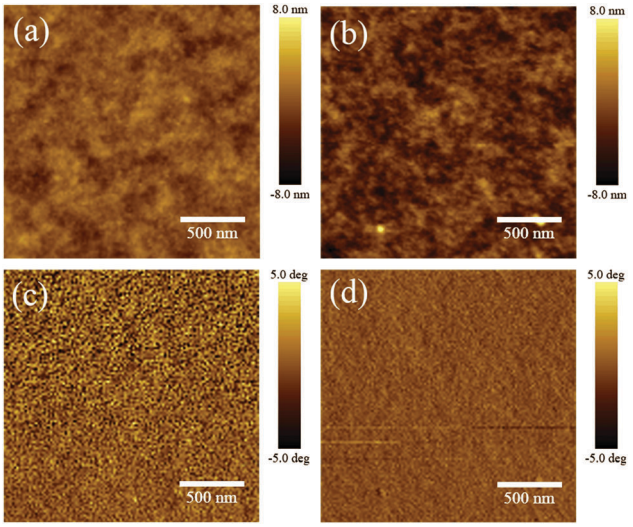

Fig. 4 AFM height (a and b) and phase (c and d) images (2 × 2 μm^2) of (a and c) PTB7-Th:PDI-2Th-PDI and (b and d) PTB7-Th:PDI-ThFTh-PDI blend films under identical fabrication conditions with photovoltaic devices.

PTB7-Th:PDI-2Th-PDI is 0.95 nm and the RMS for PTB7-Th:PDI-ThFTh-PDI is 1.37 nm (Table 2). The smoother surface is believed to be beneficial for electric contact between the active layer and the MoO_3/Ag electrode, which would help to decrease both contact resistance and leakage current.[74]

X-ray diffraction (XRD) characterization was performed to further investigate the formation of pure donor and acceptor domains in the PTB7-Th:acceptor blends. As shown in Fig. S8 (ESI†), the sharp diffraction peaks at 2θ values of $\sim 6.7^\circ$, corresponding to a d-spacing of 13.18 Å, were observed in the XRD patterns of the neat PDI-2Th-PDI and PTB7-Th:PDI-2Th-PDI blend films, implying a highly organized assembly of these π-conjugated molecules in the PDI-2Th-PDI film.[75] The pure PDI-ThFTh-PDI and PTB7-Th:PDI-ThFTh-PDI blend films did not show any obvious diffraction peaks, which indicates that the crystallinity of the PDI-ThFTh-PDI film was low.[14] These results are consistent with the AFM phase images and charge carrier mobility values of the PTB7-Th:acceptor blends. The ordered structure of PDI-2Th-PDI offers a high electron mobility, thus improving the electron transport efficiency and leading to the high J_{sc} and FF of the PSCs.

4. Conclusions

This work, for the first time, investigated the effect of bridge length on the photovoltaic properties of *ortho*-functionalized PDIs. Two novel PDI dimers with different bridge lengths were synthesized and characterized. When increasing the bridge length of the molecule, the PDI dimers showed a relatively low electron mobility and therefore poor performance. As a result, PDI-2Th-PDI with a short bridge length of 9 Å exhibited a best PCE of 4.00%, whereas PDI-ThFTh-PDI with a long bridge length of 17 Å gave a PCE of only 2.22% when they were each blended with the donor polymer PTB7-Th. Further efforts are ongoing to modify the molecular structures of PDI dimers, especially the conjugated bridge groups, for improving the photovoltaic properties of *ortho*-functionalized PDIs.

Conflicts of interest

There are no conflicts to declare.

Acknowledgements

This work was supported by the National Natural Science Foundation of China (61604101) and the Scientific Research Foundation of UESTC for Young Teacher (ZYGX2016KYQD134).

Notes and references

1 G. Li, R. Zhu and Y. Yang, *Nat. Photonics*, 2012, **6**, 153–161.
2 G. Yu, J. Gao, J. C. Hummelen, F. Wudi and A. J. Heeger, *Science*, 1995, **270**, 1789–1791.
3 T. Ameri, N. Li and C. J. Brabec, *Energy Environ. Sci.*, 2013, **6**, 2390–2413.
4 Z. He, B. Xiao, F. Liu, H. Wu, Y. Yang, S. Xiao, C. Wang, T. P. Russell and Y. Cao, *Nat. Photonics*, 2015, **9**, 174–179.
5 J. Wang, K. Liu, L. Ma and X. Zhan, *Chem. Rev.*, 2016, **116**, 14675–14725.
6 H. Li, D. He, P. Mao, Y. Wei, L. Ding and J. Wang, *Adv. Energy Mater.*, 2017, **7**, 1602663.
7 Q. Wan, X. Guo, Z. Wang, W. Li, B. Guo, W. Ma, M. Zhang and Y. Li, *Adv. Funct. Mater.*, 2016, **26**, 6635–6640.
8 K. Kawashima, T. Fukuhara, Y. Suda, Y. Suzuki, T. Koganezawa, H. Yoshida, H. Ohkita, I. Osaka and K. Takimiya, *J. Am. Chem. Soc.*, 2016, **138**, 10265–10275.
9 J. Lee, D. H. Sin, B. Moon, J. Shin, H. G. Kim, M. Kim and K. Cho, *Energy Environ. Sci.*, 2017, **10**, 247–257.
10 Y. J. Hwang, T. Earmme, B. A. Courtright, F. N. Eberle and S. A. Jenekhe, *J. Am. Chem. Soc.*, 2015, **137**, 4424–4434.
11 C. Yan, S. Barlow, Z. Wang, H. Yan, A. K. Y. Jen, S. R. Marder and X. Zhan, *Nat. Rev. Mater.*, 2018, **3**, 18003.
12 J. Zhao, Y. Li, G. Yang, K. Jiang, H. Lin, H. Ade, W. Ma and H. Yan, *Nat. Energy*, 2016, **1**, 15027.

13 K. H. Park, Y. An, S. Jung, H. Park and C. Yang, *Energy Environ. Sci.*, 2016, **9**, 3464–3471.
14 E. Zhou, J. Cong, K. Hashimoto and K. Tajima, *Adv. Mater.*, 2013, **25**, 6991–6996.
15 P. Cheng and X. Zhan, *Chem. Soc. Rev.*, 2016, **45**, 2544–2582.
16 M. Schubert, D. Dolfen, J. Frisch, S. Roland, R. Steyrleuthner, B. Stiller, Z. Chen, U. Scherf, N. Koch, A. Facchetti and D. Neher, *Adv. Energy Mater.*, 2012, **2**, 369–380.
17 X. Liu, L. J. Guo and Y. Zheng, *Nanoscale Res. Lett.*, 2017, **12**, 543.
18 T. Kim, J. H. Kim, T. E. Kang, C. Lee, H. Kang, M. Shin, C. Wang, B. Ma, U. Jeong, T. S. Kim and B. J. Kim, *Nat. Commun.*, 2015, **6**, 8547.
19 J. Hou, O. Inganas, R. H. Friend and F. Gao, *Nat. Mater.*, 2018, **17**, 119–128.
20 C. B. Nielsen, S. Holliday, H. Y. Chen, S. J. Cryer and I. McCulloch, *Acc. Chem. Res.*, 2015, **48**, 2803–2812.
21 P. Cheng, G. Li, X. Zhan and Y. Yang, *Nat. Photonics*, 2018, **12**, 131–142.
22 W. Zhao, S. Li, H. Yao, S. Zhang, Y. Zhang, B. Yang and J. Hou, *J. Am. Chem. Soc.*, 2017, **139**, 7148–7151.
23 Y. Li, J. D. Lin, X. Che, Y. Qu, F. Liu, L. S. Liao and S. R. Forrest, *J. Am. Chem. Soc.*, 2017, **139**, 17114–17119.
24 X. Liu, Y. Li, P. Huang, Y. Zhou, Z.-Q. Jiang, B. Song, Y. Li, L.-S. Liao and Y. Zheng, *J. Power Sources*, 2017, **364**, 426–431.
25 Y. Li, X. Liu, F.-P. Wu, Y. Zhou, Z.-Q. Jiang, B. Song, Y. Xia, Z.-G. Zhang, F. Gao, O. Inganäs, Y. Li and L.-S. Liao, *J. Mater. Chem. A*, 2016, **4**, 5890–5897.
26 X. Che, Y. Li, Y. Qu and S. R. Forrest, *Nat. Energy*, 2018, **3**, 422–427.
27 S. Zhang, Y. Qin, J. Zhu and J. Hou, *Adv. Mater.*, 2018, **30**, 1800868.
28 E. Zhou, J. Cong, Q. Wei, K. Tajima, C. Yang and K. Hashimoto, *Angew. Chem., Int. Ed.*, 2011, **50**, 2799–2803.
29 J. Yang, F. Chen, B. Xiao, S. Sun, X. Sun, K. Tajima, A. Tang and E. Zhou, *Sol. RRL*, 2018, **2**, 1700230.
30 E. Zhou, M. Nakano, S. Izawa, J. Cong, I. Osaka, K. Takimiya and K. Tajima, *ACS Macro Lett.*, 2014, **3**, 872–875.
31 J. Yang, F. Chen, H. Ran, J. Y. Hu, B. Xiao, A. Tang, X. Wang and E. Zhou, *Macromol. Rapid Commun.*, 2018, **39**, 1700715.
32 J. Yang, B. Xiao, K. Tajima, M. Nakano, K. Takimiya, A. Tang and E. Zhou, *Macromolecules*, 2017, **50**, 3179–3185.
33 F. Chen, G. Ding, A. Tang, B. Xiao, J. Li and E. Zhou, *J. Mater. Chem. C*, 2018, **6**, 2580–2587.
34 W. Chen and Q. Zhang, *J. Mater. Chem. C*, 2017, **5**, 1275–1302.
35 W. Li, L. Ye, S. Li, H. Yao, H. Ade and J. Hou, *Adv. Mater.*, 2018, **30**, 1707170.
36 H. Sun, X. Song, J. Xie, P. Sun, P. Gu, C. Liu, F. Chen, Q. Zhang, Z. K. Chen and W. Huang, *ACS Appl. Mater. Interfaces*, 2017, **9**, 29924–29931.
37 Z. Lu, B. Jiang, X. Zhang, A. Tang, L. Chen, C. Zhan and J. Yao, *Chem. Mater.*, 2014, **26**, 2907–2914.
38 X. Li, H. Wang, J. A. Schneider, Z. Wei, W.-Y. Lai, W. Huang, F. Wudl and Y. Zheng, *J. Mater. Chem. C*, 2017, **5**, 2781–2785.
39 X. Liu, Y. Cai, X. Huang, R. Zhang and X. Sun, *J. Mater. Chem. C*, 2017, **5**, 3188–3194.
40 Y. Zhong, M. T. Trinh, R. Chen, G. E. Purdum, P. P. Khlyabich, M. Sezen, S. Oh, H. Zhu, B. Fowler, B. Zhang, W. Wang, C. Y. Nam, M. Y. Sfeir, C. T. Black, M. L. Steigerwald, Y. L. Loo, F. Ng, X. Y. Zhu and C. Nuckolls, *Nat. Commun.*, 2015, **6**, 8242.
41 Y. Duan, X. Xu, H. Yan, W. Wu, Z. Li and Q. Peng, *Adv. Mater.*, 2017, **29**, 1605115.
42 J. Zhang, Y. Li, J. Huang, H. Hu, G. Zhang, T. Ma, P. C. Y. Chow, H. Ade, D. Pan and H. Yan, *J. Am. Chem. Soc.*, 2017, **139**, 16092–16095.
43 Z. Luo, T. Liu, W. Cheng, K. Wu, D. Xie, L. Huo, Y. Sun and C. Yang, *J. Mater. Chem. C*, 2018, **6**, 1136–1142.
44 D. Meng, D. Sun, C. Zhong, T. Liu, B. Fan, L. Huo, Y. Li, W. Jiang, H. Choi, T. Kim, J. Y. Kim, Y. Sun, Z. Wang and A. J. Heeger, *J. Am. Chem. Soc.*, 2016, **138**, 375–380.
45 J. Liu, S. Chen, D. Qian, B. Gautam, G. Yang, J. Zhao, J. Bergqvist, F. Zhang, W. Ma, H. Ade, O. Inganäs, K. Gundogdu, F. Gao and H. Yan, *Nat. Energy*, 2016, **1**, 16089.
46 H. Fu, D. Meng, X. Meng, X. Sun, L. Huo, Y. Fan, Y. Li, W. Ma, Y. Sun and Z. Wang, *J. Mater. Chem. A*, 2017, **5**, 3475–3482.
47 D. Sun, D. Meng, Y. Cai, B. Fan, Y. Li, W. Jiang, L. Huo, Y. Sun and Z. Wang, *J. Am. Chem. Soc.*, 2015, **137**, 11156–11162.
48 D. Zhao, Q. Wu, Z. Cai, T. Zheng, W. Chen, J. Lu and L. Yu, *Chem. Mater.*, 2016, **28**, 1139–1146.
49 V. Kamm, G. Battagliarin, I. A. Howard, W. Pisula, A. Mavrinskiy, C. Li, K. Müllen and F. Laquai, *Adv. Energy Mater.*, 2011, **1**, 297–302.
50 P. E. Hartnett, A. Timalsina, H. S. Matte, N. Zhou, X. Guo, W. Zhao, A. Facchetti, R. P. Chang, M. C. Hersam, M. R. Wasielewski and T. J. Marks, *J. Am. Chem. Soc.*, 2014, **136**, 16345–16356.
51 Y. Cai, L. Huo, X. Sun, D. Wei, M. Tang and Y. Sun, *Adv. Energy Mater.*, 2015, **5**, 1500032.
52 N. Liang, K. Sun, Z. Zheng, H. Yao, G. Gao, X. Meng, Z. Wang, W. Ma and J. Hou, *Adv. Energy Mater.*, 2016, **6**, 1600060.
53 X. Zhang, Z. Lu, L. Ye, C. Zhan, J. Hou, S. Zhang, B. Jiang, Y. Zhao, J. Huang, S. Zhang, Y. Liu, Q. Shi, Y. Liu and J. Yao, *Adv. Mater.*, 2013, **25**, 5791–5797.
54 J. Zhao, Y. Li, H. Lin, Y. Liu, K. Jiang, C. Mu, T. Ma, J. Y. Lin Lai, H. Hu, D. Yu and H. Yan, *Energy Environ. Sci.*, 2015, **8**, 520–525.
55 P. E. Hartnett, H. S. S. R. Matte, N. D. Eastham, N. E. Jackson, Y. Wu, L. X. Chen, M. A. Ratner, R. P. H. Chang, M. C. Hersam, M. R. Wasielewski and T. J. Marks, *Chem. Sci.*, 2016, **7**, 3543–3555.
56 Y. Duan, X. Xu, Y. Li, Z. Li and Q. Peng, *Macromol. Rapid Commun.*, 2017, **38**, 1700405.
57 Q. Wu, D. Zhao, A. M. Schneider, W. Chen and L. Yu, *J. Am. Chem. Soc.*, 2016, **138**, 7248–7251.
58 M. B. Upama, M. Wright, N. K. Elumalai, M. A. Mahmud, D. Wang, C. Xu and A. Uddin, *ACS Photonics*, 2017, **4**, 2327–2334.
59 Y. Sun, J. H. Seo, C. J. Takacs, J. Seifter and A. J. Heeger, *Adv. Mater.*, 2011, **23**, 1679–1683.

60 Z. He, C. Zhong, X. Huang, W. Y. Wong, H. Wu, L. Chen, S. Su and Y. Cao, *Adv. Mater.*, 2011, **23**, 4636–4643.
61 T. Earmme, Y. J. Hwang, S. Subramaniyan and S. A. Jenekhe, *Adv. Mater.*, 2014, **26**, 6080–6085.
62 Q. Wang, M. Wakioka and F. Ozawa, *Macromol. Rapid Commun.*, 2012, **33**, 1203–1207.
63 L. Zhang, N. S. Colella, B. P. Cherniawski, S. C. Mannsfeld and A. L. Briseno, *ACS Appl. Mater. Interfaces*, 2014, **6**, 5327–5343.
64 I. Colon and D. R. Kelsey, *J. Org. Chem.*, 1985, **51**, 2627–2637.
65 Y. Zhang, X. Guo, W. Su, B. Guo, Z. Xu, M. Zhang and Y. Li, *Org. Electron.*, 2017, **41**, 49–55.
66 F. Liu, Z. Zhou, C. Zhang, J. Zhang, Q. Hu, T. Vergote, F. Liu, T. P. Russell and X. Zhu, *Adv. Mater.*, 2017, **29**, 1606574.
67 L. Gao, Z. G. Zhang, L. Xue, J. Min, J. Zhang, Z. Wei and Y. Li, *Adv. Mater.*, 2016, **28**, 1884–1890.
68 L. Lu, W. Chen, T. Xu and L. Yu, *Nat. Commun.*, 2015, **6**, 7327.
69 W. T. Hadmojo, S. Y. Nam, T. J. Shin, S. C. Yoon, S.-Y. Jang and I. H. Jung, *J. Mater. Chem. A*, 2016, **4**, 12308–12318.
70 J. You, L. Dou, K. Yoshimura, T. Kato, K. Ohya, T. Moriarty, K. Emery, C. C. Chen, J. Gao, G. Li and Y. Yang, *Nat. Commun.*, 2013, **4**, 1446.
71 L. Chang, H. W. A. Lademann, J.-B. Bonekamp, K. Meerholz and A. J. Moulé, *Adv. Funct. Mater.*, 2011, **21**, 1779–1787.
72 W. Chen, T. Xu, F. He, W. Wang, C. Wang, J. Strzalka, Y. Liu, J. Wen, D. J. Miller, J. Chen, K. Hong, L. Yu and S. B. Darling, *Nano Lett.*, 2011, **11**, 3707–3713.
73 Q. Zhang, B. Kan, F. Liu, G. Long, X. Wan, X. Chen, Y. Zuo, W. Ni, H. Zhang, M. Li, Z. Hu, F. Huang, Y. Cao, Z. Liang, M. Zhang, T. P. Russell and Y. Chen, *Nat. Photonics*, 2014, **9**, 35–41.
74 R. Lampande, G. W. Kim, J. Boizot, Y. J. Kim, R. Pode and J. H. Kwon, *J. Mater. Chem. A*, 2013, **1**, 6895–6900.
75 Y. Liu, X. Wan, F. Wang, J. Zhou, G. Long, J. Tian, J. You, Y. Yang and Y. Chen, *Adv. Energy Mater.*, 2011, **1**, 771–775.

